On the application of magnetic methods for the characterisation of space weathering products

On the application of magnetic methods for the characterisation of space weathering products

Mark S. Bentley[i], Andrew J. Ball[ii], Ian P. Wright, John C. Zarnecki

Planetary and Space Sciences Research Institute, Centre for Earth, Planetary, Space and Astronomical Research, The Open University, Walton Hall, Milton Keynes MK7 6AA, UK

Corresponding author

Mark S. Bentley

Space Research Institute

Austrian Academy of Sciences

Schmiedlstrasse 6

A-8042 Graz, Austria

Email: mark.bentley@oeaw.ac.at

Tel: +43 (316) 41 20 657

Fax: +43 (316) 41 20 490

[i] Present address: Space Research Institute, Austrian Academy of Sciences, Schmiedlstrasse 6, A-8042 Graz, Austria

[ii] Present address: Nieuwe Rijn 28D, 2312 JD Leiden ZH, The Netherlands

Abstract

Space weathering is now commonly accepted to modify the optical and magnetic properties of airless body regoliths throughout the Solar System. Although the precise formation processes are not well understood, the presence of ubiquitous sub-microscopic metallic iron (SMFe) grains in lunar soils and corresponding spectral analyses have explained both the unique optical and magnetic properties of such soils. More recently, a variety of ion irradiation, laser melting and vaporisation and impact experiments have been shown to reproduce these effects in the laboratory. Such experiments are crucial to the study of the formation of SMFe under controlled conditions. To date, more emphasis has been placed on optical analyses of laboratory samples, as these address directly the mineralogical interpretation of remote sensing data. However, the magnetic analyses performed on the *Apollo* and *Luna* samples have provided useful qualitative and quantitative evaluation of regolith metallic iron content. These techniques are reviewed here, demonstrated on pulsed laser irradiated olivine powder, and their utility for determining the quantity and size distribution of this metallic iron discussed. Ferromagnetic resonance, multi-frequency magnetic susceptibility, vibrating sample magnetometry and thermomagnetic measurements were carried out. Each showed trends expected for the conversion of paramagnetic Fe^{2+} in olivine to fine-grained Fe^{0}, with some grains in the superparamagnetic size range. Although evidence for superparamagnetic iron was found, the quantity of sub-microscopic metallic iron produced in these experiments proved insufficient to make conclusive measurements of either the quantity or size distribution of this iron. Improvements to both the experimental and analytical procedures are discussed to better enable such measurements in the future.

Keywords: space weathering, planetary regolith, magnetic measurements

1. Introduction

Space weathering on the Moon (and by analogy possibly other airless rocky bodies such as Mercury and certain asteroid types) is now generally accepted to be caused by the reduction of ferrous iron to fine grained metallic iron during impacts and ion irradiation. In the lunar regolith, fine-grained iron (often termed SMFe, for sub-microscopic metallic iron) is found in two distinct locations – in amorphous coatings and in agglutinates.

It has long been known that lunar soils have an "excess" of metallic iron relative to the rocks from which they are derived (Fuller et al., 1975) and that the magnetic fraction of lunar soils appear darker and redder than the non-magnetic fraction (Hapke, 2001). More mature soils were found to have a higher fraction of agglutinates, a lower albedo, and the ferromagnetic resonance (FMR) signature I_s/FeO, a proxy for soil maturity, correlated well with other maturity indices (Morris, 1976). Thus SMFe bearing agglutinates were thought responsible for the unique optical and magnetic properties of lunar soils. Early studies of *Apollo* samples looked at the size distribution of SMFe in agglutinates, where the size ranged from 0.4 to 25 nm, with a peak in the mass fraction at 12.5 nm (Housley et al., 1973). More recent studies used BSE-SEM techniques to measure the size distribution in the range 10-1500 nm; the mean SMFe size per sample varied from 44-544 nm (James et al., 2003).

Modern TEM techniques later revealed reduced metallic iron particles to be ubiquitous components of almost every grain in mature lunar soil samples, with nearly every grain having metallic iron within the first 100 nm of the surface (Keller et al., 2000). The iron found in such amorphous grain coatings is typically a few nanometres in diameter (Wentworth et al., 1999; Keller and Clemett, 2001), somewhat smaller than that in agglutinates. In addition, reflectance spectra of lunar soil separates (Pieters et al., 1993) revealed that the bulk optical properties of the soil are most similar to the finest fraction. This was explained by noting that despite the small mass fraction that these particles represent, they have a very high surface area, favouring a surface-correlated source of iron.

Thus there has been some debate over the relative importance of agglutinates, which can form a large fraction of a mature lunar soil and are known to be SMFe rich, and vapour deposits in the role of space weathering. The most likely scenario is that SMFe forms as nanometres spherules at grain surface (either by melting or vapour deposition) and that during the formation of agglutinates, which are themselves products of

the finest fraction, this iron is bound into agglutinates and undergoes coarsening (Pieters et al., 2000). Basu et al. (2003) for example, analysed over a thousand grain rims and concluded that in mature soils the SMFe is mainly bound in agglutinates, although its origin may have been as vapour deposits.

Modelling the spectral changes caused by SMFe has shown that the effects typically ascribed to space weathering (reddening, darkening and reduced spectral contrast) can in many cases be explained by the optical properties of iron grains smaller than the wavelength of observation (Hapke, 2001). Recent work with nanophase iron analogue materials has shown that there is a transition at an iron spherule diameter of about 50 nm between Rayleigh scattering (strongly reddening) and non-Rayleigh scattering (darkening, but little reddening) (Lucey & Noble 2008). By creating sets of such analogues with different iron sizes, Noble et al. (2007) demonstrated that the smallest particles (5-15 nm) strongly affect visible reflectance, even at low concentrations, but that strong reddening does not occur until a significant amount (> 1wt%) of iron is present. For larger (25-50 nm) iron spherules, reddening is found at much lower concentrations, and adding more iron results in a linear spectrum. For larger yet grains, the visible part of the spectrum is less affected but a significant slope is found in the infrared. Reflectance spectra of lunar soils most closely match the 10-25 nm weathering analogue, and yet the size of SMFe in amorphous grain coatings is around 3 nm. Thus it appears that SMFe in both agglutinates and grain rims are important for producing the lunar spectra.

The precise nature of the processes forming SMFe is poorly understood, but laboratory studies have suggested several viable mechanisms for the production of nanometre sized iron grains. In materials with existing large grained iron, it has been shown that this can be disseminated into fine-grained Fe^0 during impact events (Hörz et al., 2005). To demonstrate this, the authors comminuted an ordinary chondrite and then used the resulting powder in flyer-plate impact experiments at a variety of impact velocities and pressures. The resulting silicate melts were found to contain abundant Fe^0 particles of <100 nm in size.

For materials without native metallic iron, reduction of Fe^{2+} to Fe^0 has been demonstrated in a variety of ways. Moroz et al. (2009) analysed glasses produced using both a μs pulsed laser and resistance furnace to melt samples of a martian soil analogue under vacuum conditions. The laser irradiated samples produced amorphous glass containing 25-80 nm diameter metallic iron spherules. Pulsed laser simulations with a shorter pulse-width of 6-8 nm, thought to simulate impact vapour deposition, also successfully produced nanophase iron (Sasaki et al., 2001). In these experiments, olivine samples were irradiated and the resulting

grains were found to have ~200 nm thick amorphous rims containing metallic iron spherules of up to 30 nm in diameter.

Energetic ions are also known to cause space weathering effects; the deposition of energy in this way causes amorphisation of the outer layers of grains and also sputtering from their surface. Irradiation by a variety of ions in the laboratory has been used to simulate the effects of the solar wind on various minerals. Yamada et al. (1999) irradiated pellets of powdered olivine and orthopyroxene with 1 MeV protons (considerably higher than typical solar wind energies). While they saw almost no change in the pyroxene samples, the olivine did indeed show spectral trends similar to those ascribed to space weathering. Loeffler et al. (2009) also irradiated olivine, but with helium ions at 4 keV, and monitored the NIR reflectance spectra and chemical composition during irradiation. In addition they measured surface elemental abundance using X-ray photoelectron spectroscopy to determine the fraction of surface iron in the metallic form, and demonstrated that it correlated with the degree of spectral reddening. Finally, they determined that partial oxidation of this iron occurred after removal from the vacuum chamber, and also that reduction to metallic iron can occur through direct ion bombardment, and not only via re-deposition of sputter products. Thus there are a variety of mechanisms that can produce fine grained metallic iron, all of which probably operate with different efficiencies.

As well as being responsible for the optical effects of weathering on the Moon, evidence for the reduction of Fe^{2+} to fine-grained metallic iron in an olivine rich martian meteorite has also been recently presented (Van de Moortèle et al., 2007). Microscopic analysis found evidence of Fe and FeNi particles of 3-30 nm in size, in agreement with the results of magnetic analyses. Optical analysis of this same meteorite (Pieters et al., 2008) shows that the unusual visible and near-infrared reflectance characteristics of this sample are in good agreement with the results of experimentally produced space weathering analogues comprising a variety of nanophase iron sizes (Noble et al., 2007).

To summarise, the quantity, size distribution and location of SMFe particles (on grain surfaces, or in agglutinates) must be understood in order to study of space weathering analogues, lunar soils and potentially future returned samples or in-situ analyses. In order to overcome the limitations of TEM analyses and obtain meaningful statistics on bulk samples, magnetic techniques can be considered to probe the quantity and grain size of metallic iron.

To study the magnetic properties of weathered regolith analogues, laser irradiation was used to weather mineral samples artificially. Measurements including magnetic susceptibility, electron spin resonance and vibrating sample magnetometry were performed on the samples, alongside the usual reflectance spectroscopy, to evaluate the potential of these techniques in better understanding space weathering. The experimental setup and analysis techniques are described in the following sections, and the results discussed in the context of their ability to measure the amount and size distribution of iron.

2. Artificially weathered regolith analogues

Laboratory experiments have been performed to evaluate the effects of hypervelocity impacts (HVI) and light ion sputtering on Solar System materials for several decades (e.g. McDonnell et al. 1972). Ion irradiation with a variety of species and energies can be performed with relatively standard facilities. Simulating impacts is a little more difficult. Both light gas guns (LGGs) and electrostatic Van de Graaf (VdG) accelerators can be used in the laboratory, however guns produce particles with a speed typically too low to produce significant vaporisation, and at too low a rate to be useful. Accelerators have neither of these problems, but are restricted to firing electrically conductive particles, commonly iron. Since space weathering is critically dependant on the presence of fine-grained iron this contamination was considered too severe. In the interim, techniques have been developed to allow silicate minerals to be coated with a conductive layer and hence accelerated (e.g. Hillier et al. (2009)), however dust accelerators still provide only a limited dust flux that would result in prohibitively long exposure times.

Recent experiments have demonstrated pulsed lasers as a proxy for micrometeorite impacts in space weathering simulation (Sasaki et al., 2001). In this case the aim is not to replicate the cratering process, for which the ablation pressure is matched to the impact over-pressure (Hill, 1990), but instead to simulate the heating and subsequent melting and vaporisation caused by a rapid and localised deposition of energy. The advantages of this technique are clear – it is simple, versatile, can operate with high repetition rates and is contaminant-free. It is, however, difficult to calibrate accurately a laser generated “impact” with the mass and velocity of a real event. So while there is clear evidence for SMFe being produced in such experiments, it is difficult to calculate weathering and exposure rates from them. Nevertheless, this is the approach adopted here.

The parameters of the simulation were originally chosen to approximate conditions on Mercury, soon to receive its first three orbiting spacecraft, MESSENGER (Solomon et al., 2001) and the *BepiColombo* MPO and MMO (Anselmi and Scoon, 2001). In defining the pulsed laser simulation, three assumptions were made: that the spot size of the beam should be equal to the projectile diameter, that the pulse duration should equal the duration of the impact compression phase, and that the energy deposited in the sample target should be similar in both cases. The experimental parameters chosen, and their rationale, are given below.

The mass distribution of dust particles at Mercury has been shown to be dominated by the range 10^{-5} to 10^{-7} g, accounting for approximately 75% of the flux by mass (Müller et al., 2002). The density of IDPs is not well constrained, but a quick calculation shows that for a spherical particle with mass 10^{-6} g the calculated particle diameter only varies from 100 to 128 μm if the density is either solid iron or water ice (neglecting porosity). Hence a spot size of order 100 μm is appropriate.

The compression phase of an impact is said to be complete when the shock wave reaches the rear of the projectile. Thus the duration of this phase can be calculated if the shock speed and the projectile size are known. The shock speed was calculated using the planar impact model (Melosh, 1989) and linear equation of state (EOS) for a variety of materials, including basalt, anorthosite and a typical regolith. Using the particle size given previously, this approach yields compression durations in the range 5 to 6 ns. Thus a typical Nd:YAG Q-switched laser with a pulse duration of 10 ns was judged to be adequate for these experiments.

The pulse energy is by far the most uncertain of the quantities needed to define a space weathering experiment of this type. The Divine dust flux model (Divine, 1993) was used to calculate the impact energy flux over the surface of Mercury as a function of mass and velocity. A plot of the kinetic energy flux for the maximum flux case is shown in Figure 1. Mercury's high eccentricity results in an impact velocity and hence energy flux that changes considerably over its orbit, however the maximum value is always found for a micrometeorite mass/speed combination of 10^{-6} g and 32 km s^{-1}, resulting in a single impact kinetic energy of 0.512 J. Applying the planar impact model again and using a hypothetical impact of an iron projectile onto a regolith target, for which values of the threshold melt and vaporisation pressures are available, the peak pressure at this impact velocity would certainly result in vaporisation at the point of impact (see, for example,

Cintala (1992)). The volume of vapour depends on the rate at which this pressure decays from the point of impact in both the target and projectile.

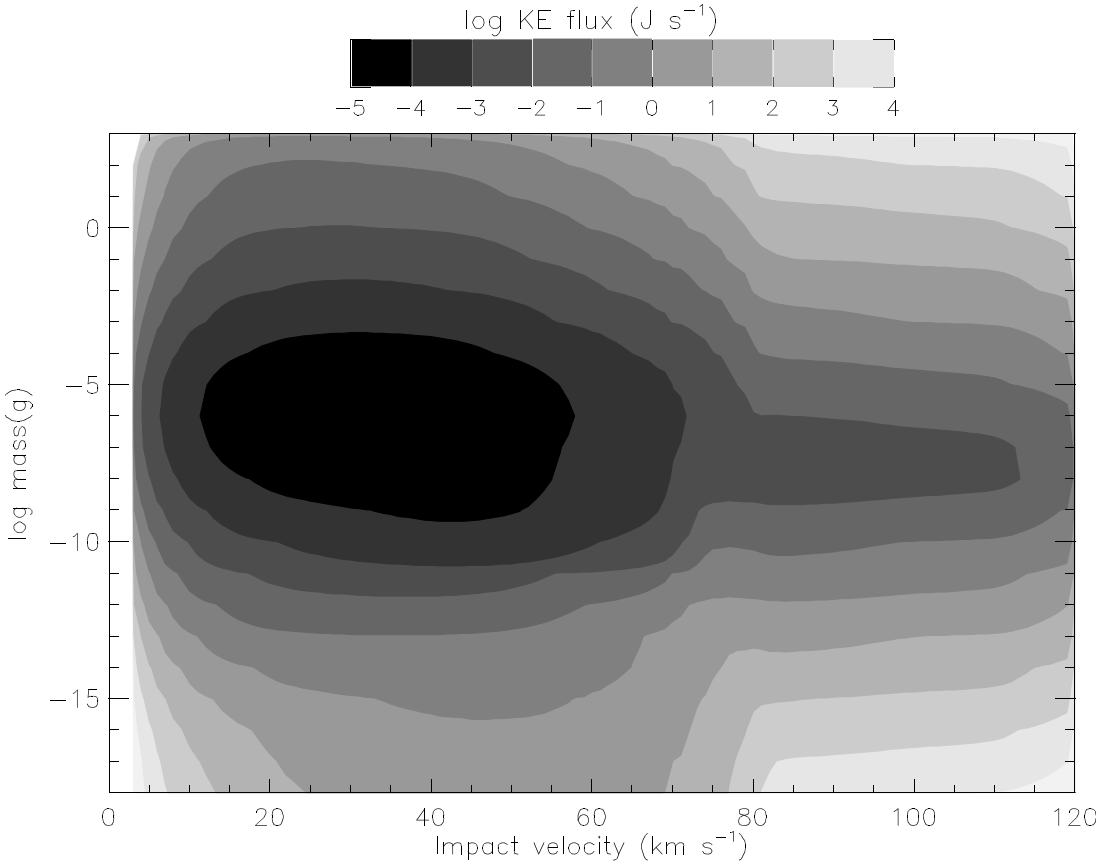

Figure 1. A contour plot showing the kinetic energy flux over the surface of Mercury. The maximum energy flux is 25 J s^{-1} for micrometeorites with a mass of order 10^{-6} g and a velocity of 17 km s^{-1}.

The difficulty arises in translating this impact kinetic energy to a corresponding laser energy, taking into account the different energy and momentum transfer mechanisms. The laser ablation process is complex, generating plasma that absorbs subsequent radiation, leading to very high ablation pressures. To compare impacts to laser pulses quantitatively requires models of both hypervelocity impact and laser ablation. Using such a method, Pirri (1977)) calculated laser parameters for the impact of water onto graphite. They showed that a 1064 nm laser pulse with an energy of order 2 J and a duration of order 20 ns would simulate the pressure of an 80 μm radius projectile impacting at a speed of 6 km s^{-1}, corresponding to an impact kinetic energy of only 0.077 J . This approach employed the principle of late-state equivalence, which states that if the flow and pressure fields for two impacts are the same, the subsequent craters will be identical. As a result, the energy deposition process can be significantly different, provided that the pressures produced are

identical. This approach therefore yields the energy required to produce a similar crater, not necessarily to produce a similar degree of melting and vaporisation, which could be achieved by a different combination of parameters.

This was further demonstrated by Kissel and Krueger (1987), who compared laser pulses with real dust impacts and showed that the mass spectra and ion yields for a 1 μm particle with an impact speed of 15 km s^{-1} could be reproduced by a laser pulse with a flux between 10^8 and 10^9 W cm^{-2}. The flux required to achieve similar crater scaling, however, was considerably higher (approximately 10^{11} W cm^{-2}). Matching the ablation and impact pressures is therefore not considered here to be an essential technique for defining laser parameters to simulate space weathering. Rather, it is more important to match the yields of vaporisation and ionisation, since it is these rates that drive the space weathering process.

The relationship between laser energy and impact speed has also been studied experimentally by analysing the vapour plume generated by a pulsed laser (Kadono et al., 2002). Using thermodynamic models of vapour expansion and fitting to experimental data, the authors found that a laser intensity of 1.3×10^{10} W cm^{-2} (derived from a laser pulse with 380 mJ energy, 500 μm spot size and 15 ns duration) equated to the collision of two basaltic objects at approximately 120 km s^{-1}. Unfortunately their experiments were carried out at a single laser energy and so it is not possible to extend these results to find the energy necessary to simulate the much lower average Solar System impact speeds. However, it can be taken as an upper limit.

A lower limit on the laser energy can be found from the requirement that the power density shall be sufficiently high to vaporise the target material, and was given above as between 10^8 and 10^9 W cm^{-2}. No precise relationship can therefore be defined at this stage between the energy of a typical micrometeorite impacting Mercury and the laser pulse energy required to achieve similar melt and vapour production. However, the power density should fall in the range 10^8 to 10^{10} W cm^{-2}.

Above the energy threshold required to produce vapour, the mass of vapour created in an impact is known to increase in proportion to the impactor mass and the square of the speed (Melosh, 1989), i.e. to the kinetic energy of the projectile.

The wavelength of the laser is also of interest. The first experiments used Nd:YAG IR lasers operating at their fundamental frequencies. However, successful experiments have also operated in the UV (Brunetto et al., 2006). In this regime it is expected that a different physical mechanism operates but operation in the infrared is still believed here to be the best simulation of the heating, melting and vaporisation caused by a micrometeorite impact. The ideal laser parameters, as derived above, are summarised in Table 1.

Laser Parameter	Parameter range
Wavelength	1064 nm
Pulse duration	10 ns
Power density (P)	10^8 W cm^{-2} < P < 10^{10} W cm^{-2}
Spot diameter	Ideal: 100 µm Achieved here: 1 mm

Table 1: Laser parameters approximating a typical micrometeorite impact on Mercury.

3. Experimental setup

The experimental setup is presented in Figure 2. The vacuum chamber was evacuated to better than 10^{-6} mbar using a rotary backing and a turbo-molecular pump. A foreline trap was used to remove pump oil and heater tape was used regularly to bake out the chamber.

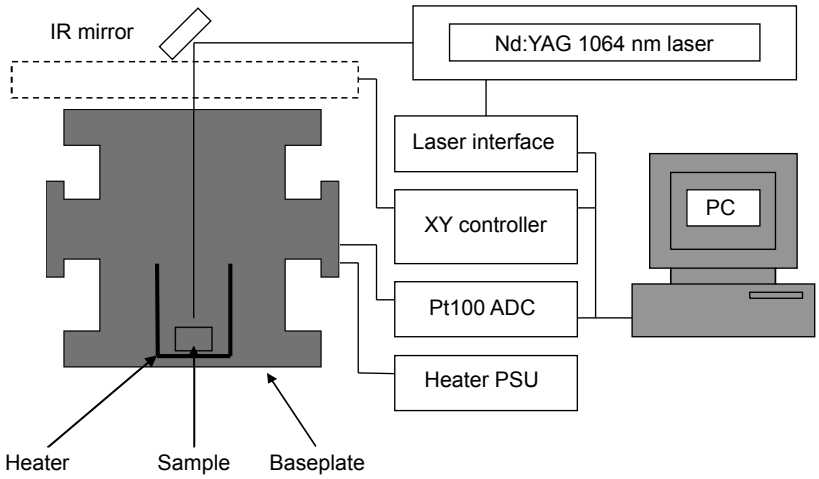

Figure 2. Schematic of an experimental setup to artificially space weather a sample under vacuum and at a range of temperatures via pulsed laser irradiation.

Samples were temperature-controlled to investigate the effects of bake-out, and of the sample temperature on the quantity and size distribution of SMFe, as these are particularly interesting parameters for Mercury (Noble and Pieters, 2003). Samples were thus heated in a custom Macor pot, which was machined as a former for a coil of Nichrome wire. The coil was wound in a bifilar configuration to reduce the magnetic field applied to the sample and minimise the impact on subsequent magnetic analyses. A future improvement would be to heat the sample radiatively and measure its temperature via thermal IR. Sample temperature was estimated here from a flat film Pt100 sensor mounted in the base of the pot and read in a 4-wire configuration.

The laser used was a Spectron SL-401 Nd:YAG operating at 1064 nm. Due to damage to the laser rod, a perfectly symmetrical TEM_{00} beam was not produced, and difficulties were found in focussing the beam much below 1000 μm and so this spot size was adopted for all experiments, rather than the desired diameter of 100 μm. Given the other approximations necessary in parameterising this simulation, this was not judged to be a serious problem. The laser was typically fired at a frequency of 5 Hz and average pulse power was derived from measurements using a commercial continuous wave (CW) power meter. A pulse energy of between 20 and 30 mJ per pulse was adopted for most experiments. This results in an energy density of approximately 4×10^8 W/cm^2 and should result in partial melting and vaporisation of the olivine grains. As a result it was hoped that SMFe would be produced either in a thermal or vapour re-deposition process.

To produce sufficient metallic iron to produce measurable changes in both the optical and magnetic properties of the regolith analogue, it was necessary to irradiate the sample repeatedly in a uniform manner. An optical window was fitted to the top port of the chamber to allow the sample to be exposed to the laser. A computer–driven set of stepper motors controlled the beam position via two mirrors. Custom software controlled the laser, beam controller and logged temperature data.

After irradiation, samples were allowed to cool to room temperature before the chamber was brought to ambient pressure and the sample removed. Some concern was given to the possible oxidation of fine-grained metallic iron after removal from the vacuum system, but previous experimenters have shown that laboratory weathered samples appear stable over extended periods, and indeed lunar soil samples show no signs of extensive oxidation at room temperature (Greenwood and Howe, 1970).

During a typical experiment the chamber pressure was observed to spike during laser firing, and some particles were seen to be ejected from the sample container. However, no thermal imaging or high speed video were available to show evidence of a vapour plume. Unfortunately no mineralogical analysis was performed on the samples and hence no direct evidence of melting or vaporisation was seen. The overall irradiation experiment is rather similar to that of previous experimenters (Sasaki et al., 2001); (Yamada et al., 1999) with the exception that powders, rather than pellets, are used, and so similar results are expected.

4. Sample materials

The mineralogy of Mercury's surface was poorly constrained at the time of these experiments, although upper limits on the amount of Fe^{2+} had been deduced. The lack of obvious ferrous iron features in the visible and near-infrared reflectance spectra can be interpreted either as a lack of ferrous iron in the crust, or the action of a lunar-like space weathering process that acts to reduce iron to a metallic form. MESSENGER has since performed several Mercury fly-bys; the first two confirmed the low quantity of ferrous iron-bearing minerals (Blewett et al., 2009). During the third flyby, however, initial measurements of elemental abundance from the neutron spectrometer showed a significant amount of iron, although probably not bound in silicate minerals.

In the first instance, however, samples of olivine were preferred, because they have been shown to weather readily (Yamada et al., 1999); San Carlos olivine was thus chosen. The relative weathering rates of different minerals are of course of great interest in themselves. If the mechanisms previously described are responsible for space weathering, then the Fe-O bond strength presumably plays an important role in controlling this rate; studying this via experiments with different minerals should help interpretation of observed weathering rates. Further experiments should be performed once MESSENGER has provided further constraints on the surface composition and mineralogy.

A silica sand with a very low iron content, typically used for commercial glass manufacture, was also obtained to confirm that the presence of ferrous iron was responsible for the changes observed.

Most previous experiments have used pressed pellets of powdered material. This can simplify some experimental difficulties (for example it enables horizontal mounting of samples, which can be useful for

some beamlines), however it is not as representative of reality. Here it was desired to use powders, since this more closely represents a sample of natural regolith. It also allowed samples to be subdivided easily for multiple analyses. The San Carlos olivine was received in the form of ~1 cm chips. Optically dark inclusions were visible in some chips and a selection of those with no visible inclusions was made. These chips were crushed in a Temar and dry sieved to 5 φ (63 μm); mid-infrared observations of Mercury have been interpreted as being best fit by a regolith with typical grain sizes of 30 μm (Sprague et al., 2002).

A representative sample of olivine was analysed on a Cameca SX100 microprobe, giving an FeO weight percentage of 9.65%, and a forsterite number (molar Mg/(Mg+Fe) × 100) of Fo_{90}.

5. Optical analyses

An olivine sample uniformly irradiated with several thousand 30 mJ laser pulses showed a visible darkening, although not as prominent as that reported by Yamada, Sasaki et al. (1999). This is probably because the sample used here is unconsolidated and is in fact "turned over" in much the same way as the lunar regolith is gardened, but here by the generation of vapour or plasma during the laser shots. This lofting of the sample powder is visible during irradiation and results in some loss of material from the container. There is therefore a "boundary effect" that must be corrected for in any quantitative analysis of weathering rates using this technique. All samples were weighed before and after irradiation to correctly calculate the magnetic properties. Since not all grains in a given sample are exposed, and yet each sample was sub-sampled for further analysis, care was taken to well mix the recovered powder – again reducing the effect relative to a pellet sample.

Bi-directional visible to near-infrared reflectance spectra of this powdered material were recorded at the RELAB facility, operated by Brown University on behalf of NASA (Pieters and Hiroi, 2004). Spectra were acquired at an incidence angle of 30º and an emergence angle of 0º relative to a pressed Halon (Lambertian) standard in the same geometry. The absolute spectra of the olivine sample before and after laboratory weathering are shown in Figure 3. Also plotted is the spectrum of the irradiated material, scaled to match the reflectance of the unaltered material at a wavelength of 560 nm in order to see the increased spectral slope in the NIR. Thus spectral reddening and an overall reduction in albedo are immediately visible. A reduction in spectral contrast is also seen in lunar space weathering. If a simple straight line continuum is fitted in the NIR on either side of the 1 μm band, the band depth can be calculated as $1 - R_b/R_c$ where R_b is

the reflectance at the centre of the band, and R_c the reflectance of the continuum at the same wavelength (Clark and Roush, 1984). This shows that the band depth decreases from 0.48 to 0.43, demonstrating the reduction of spectral contrast in the infrared.

It should be recalled that these samples were “bulk” powders rather than pellet samples, and so the optical changes are less marked than would be expected from a consolidated sample; nevertheless all of the expected changes are evident. It would be interesting to perform optical analyses on magnetic separates of these samples. This should give similar results as for *Apollo* samples, in which the magnetic fraction dominates the bulk optical properties. Similarly, it would also be interesting to perform acid leaching experiments on the irradiated samples to confirm the surface correlated nature of the changes in both optical and magnetic properties.

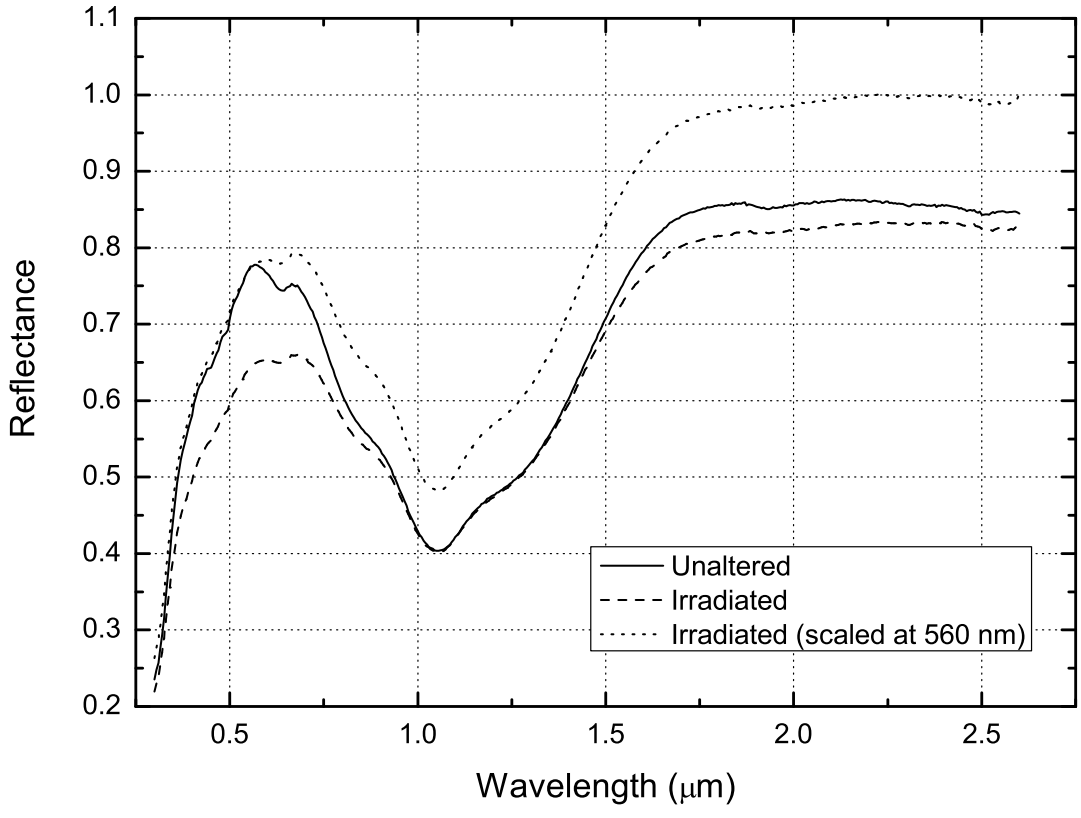

Figure 3: VNIR reflectance spectra of weathered and un-weathered olivine samples. The darkening and reduction of spectral contrast are clearly visible. Also shown is the weathered spectrum scaled at 560 nm to demonstrate the reddening.

Finally, it should be recalled that similar spectral changes can also be caused by absorption from Fe^{3+} in a silicate glass (e.g. (Cloutis and Gaffey, 1993)) and thus attempts must be made with the subsequent analyses to exclude this possibility.

6. Magnetic analyses

All of the magnetic techniques described here rely on that fact that metallic iron is ferromagnetic, and that it is the dominant magnetic phase in the lunar regolith. Although it is by no means certain, this may also be the case at Mercury and some asteroids types. The reducing environment of airless planetary surfaces, and hence the lack of ferric iron, makes the magnetic mineralogy of the Moon somewhat different from that of the Earth, which is dominated by titano-magnetites. Early analyses of the lunar samples showed that metallic iron is by far the most dominant magnetic mineral, being present in lunar rocks at a level of 0.1 wt%, and in soils at 0.5 – 1.0 wt% (Nagata et al., 1972). This enhancement in the soils is a direct result of space weathering.

6.1. Bulk magnetic susceptibility

Measurements of bulk magnetic susceptibility of lunar rocks and soils demonstrate that a simple in situ measurement should be a useful indicator of weathering. The advantage of such a measurement is that it can be made rapidly and non-destructively, it is rather non-specific, however. The application of magnetic susceptibility to measurements of regolith maturity has previously been discussed (Bentley et al., 2009) and only a brief overview will be given here. In short, magnetic susceptibility represents how readily a material can be magnetised, and is defined as the ratio of magnetisation to applied field. It is dimensionless in SI units, but mass-specific susceptibility is also often used, in which the volume susceptibility is divided by the density of the material, to give units of $m^3\ kg^{-1}$.

The magnetic type of a material is readily determined by this simple measurement – purely diamagnetic materials have a small but negative susceptibility, paramagnetic materials have a small and positive magnetic susceptibility and ferromagnetism is a special case of paramagnetism in which atoms with a net magnetic moment are closely packed in a lattice, resulting in interaction between atomic moments and a cooperative alignment known as spontaneous magnetisation. Such materials can maintain their magnetisation even in the absence of an applied field.

Ferromagnetic materials have a magnetic susceptibility considerably higher than paramagnetic ones, but their susceptibility is a function of the magnetic grain size and applied field (see, Bentley et al. 2009) for a discussion of the effect of magnetic grain size on susceptibility for metallic iron). It is these effects that make magnetic techniques both useful but complex to analyse. Table 2 lists typical values of initial magnetic susceptibility for some typical terrestrial and lunar materials.

Material	**Formula or comment**	**Mass susceptibility (10^{-8} m^3 kg^{-1})**
Fayalite	Fe_2SiO_4	12
Quartz	SiO_2	-0.63
Terrestrial basalt	Function of titano-magnetite content	25 – 12,000
Lunar soil	Depends on maturity	1382 - 4398
Lunar basalt	Variation much smaller than terrestrial basalt	63 - 880

Table 2: Tabulated values of typical mass magnetic susceptibility for a selection of lunar and terrestrial materials (Carmichael, 1989).

In the case of space weathering, the conversion of paramagnetic ferrous iron (Fe^{2+}) in the olivine into ferromagnetic metallic iron (Fe^0) should produce an increase in the bulk magnetic susceptibility, regardless of the size and hence domain state of the produced iron. The magnetic susceptibility of olivine is known to vary in a non-linear way with iron composition, from the diamagnetic behaviour of pure forsterite (containing no iron) to fayalite, which is paramagnetic with a mass susceptibility of 1.10×10^{-6} m^3 kg^{-1} (Belley et al., 2009). The magnetic susceptibility of Fo_{90} should be approximately 0.2×10^{-6} m^3 kg^{-1}.

Measurements of initial magnetic susceptibility (that is, measurements at a low applied field strength, such that the sample magnetisation is reversible) were carried out using a Bartington MS-2B instrument. This generates a low intensity (~250 μT peak) magnetic field by energising a coil with alternating current at a frequency of 0.465 kHz (there is also a higher frequency mode, which will be discussed later). The frequency

is sufficiently low that conductive losses are minimised. When a sample is brought within range of this coil, the inductance is changed and the frequency of the oscillator changes with it. This change in coil inductance relates to the change in relative magnetic permeability (μ_r) and hence susceptibility ($\mu_r = 1 + \kappa$) of the sample. Since this is a relative measurement (i.e. relative to free space), the meter must be zeroed immediately before each reading, with no sample present.

Several sub-samples of un-irradiated olivine were first measured and found to have the same susceptibility, within measurement errors[iii]. A value of $17.29 \pm 0.07 \times 10^{-8}$ m^3 kg^{-1} was recorded, which compares very favourably with the published value for pure Fo_{90} (Belley et al., 2009).

A sample of ~5 g of olivine was irradiated with about 7000 laser pulses of 15 mJ pulse energy. After irradiation, the bulk initial susceptibility, recorded in the low frequency mode, was seen to increase by $8.79 \times 10^{-8} \pm 0.09$ m^3 kg^{-1} (from 17.29 ± 0.07 to $26.08 \pm 0.05 \times 10^{-8}$ m^3 kg^{-1}). Additional scans further increased the susceptibility, but by smaller increments, suggesting a saturation effect. This has not yet been fully explored.

To confirm the dependence on ferrous iron, a sample of silica sand with a low iron content, reported as 0.029%, was acquired. This sample, typically used in glass manufacture, was ground and sieved such that the particle size distribution was similar to that of the olivine sample. The unaltered sample showed a small negative susceptibility, as is expected for a relatively pure paramagnetic material. This sample underwent the same irradiation procedure as for olivine and the susceptibility was again measured. Within measurement errors, the values for irradiated and non-irradiated quartz were found to be identical.

This lends credence to the argument that the space weathering simulation is in fact reducing ferrous iron to its metallic form, but it is not uniquely diagnostic of it. Increases in magnetic susceptibility could also be caused by the production of iron oxides. However, it was noted that when the irradiation is carried out in air, and not under vacuum, the increase in susceptibility is negligible. This could be taken as evidence that a

[iii] Each sample was transferred to a diamagnetic glass bottle whose susceptibility was known. The Bartington instrument was allowed to warm for 30 minutes and measurements were performed well away from any metallic surfaces that could cause interference. An average reading was then acquired of several measurements.

reducing environment is required to facilitate this change, however there are other factors that could also play a role, for example the slower cooling of melt in vacuum.

In conclusion measurement of initial magnetic susceptibility at a single frequency and temperature cannot distinguish between different magnetic carriers, but could be useful once magnetic minerals have been identified to provide a rough assessment of their quantity. Therefore the magnetic components in any sample should first be identified, something often done by thermo-magnetic analysis (TMA).

6.2. Thermo magnetic analysis

High temperatures can disrupt the spontaneous magnetisation of ferromagnetic materials. Beyond a critical temperature (the Curie temperature), materials behave once more like a simple paramagnet. In practise, this means that the magnetic susceptibility of such a material shows a sharp drop at this temperature and this can be used to identify magnetic carriers in a sample; the Curie point of metallic iron is 1040 K.

A KLY-3 “Kappabridge” magnetic susceptibility bridge fitted with a CS-2 furnace was used to make this measurement, with a constant argon purge to reduce oxidation at high temperatures. This instrument uses an AC susceptibility bridge operating at a frequency of 875 Hz.

The thermo-magnetic curves (Figure 4) show primarily paramagnetic behaviour, as seen by the Curie-law decrease in susceptibility with temperature; no obvious Curie point was observed at the expected temperature of 1040 K. However, there is a definite change between the un-irradiated olivine and the weathered sample. The irradiated sample shows an overall higher magnetic susceptibility, however this enhancement appears to disappear after heating.

It is known from the lunar case that preventing oxidisation of metallic iron during these experiments is difficult; Dunlop and Özdemir (1997) suggest that above about 950 K, even a high-vacuum system cannot prevent oxidation of fine-grained metallic iron and samples must be heated in a regulated H_2-N_2 mixture. Measurements of the Curie temperatures of lunar regolith samples have been obtained by sealing the samples in evacuated quartz tubes prior to analysis (e.g. Stephenson, 1971b), but this could not be readily accommodated in the Kappabridge. Production of fine-grained metallic iron during irradiation, and subsequent re-oxidation on heating is one possible explanation for the results here.

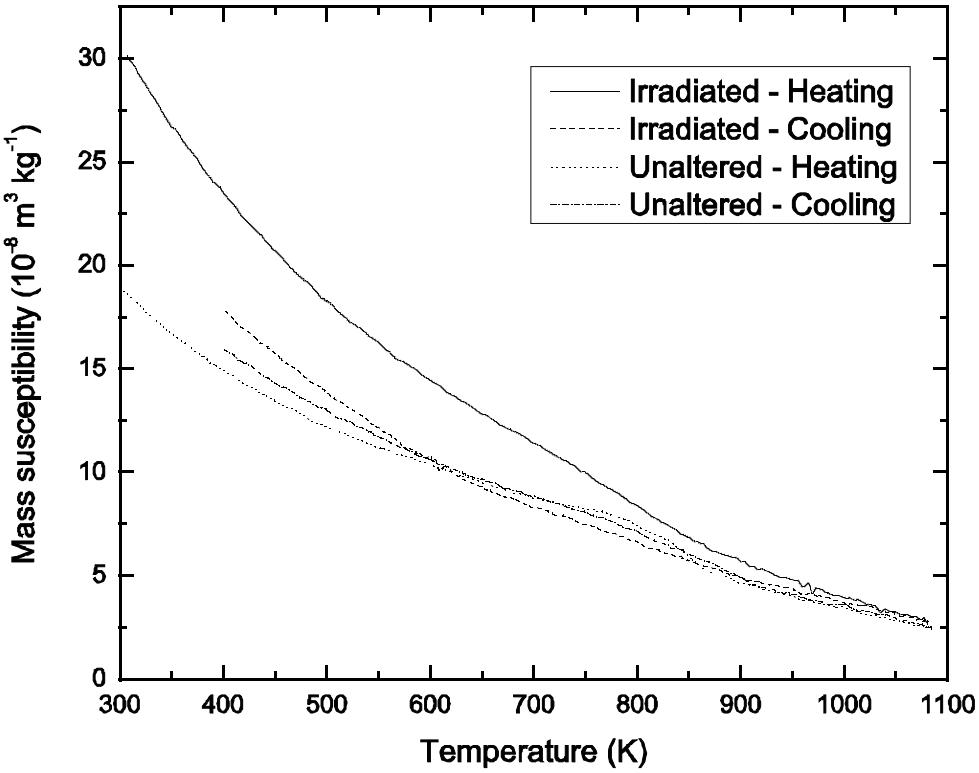

Figure 4: Thermomagnetic analyses of an artificially weathered, and unaltered olivine sample during both heating and cooling.

The heating curve of the original olivine sample also appears to show a possible magnetic contaminant by the “shoulder” seen around 750 - 800 K. For weakly magnetic materials, the plot of susceptibility versus temperature is the sum of two components - a simple hyperbolic element from the paramagnetic component, given by the Curie law, and the more complex behaviour due to the ferromagnetic component. It is known that from room temperature to several hundred degrees, the ferromagnetic component is described well by either a constant or a very shallow susceptibility gradient (Hrouda, 1994). In this regime it is therefore possible to fit a hyperbolic function to the data in order to determine the Curie constant. The paramagnetic contribution can then be subtracted from the data to leave the ferromagnetic component. This has been done in Figure 5, which shows the thermomagnetic analysis of just the magnetic component, resulting in a distinct drop in magnetic susceptibility in the range of 775 to 875 K. Magnetite has a Curie temperature of approximately 850 K, and in the titanomagnetites series this drops with increasing titanium content (Dunlop

and Özdemir, 1997), therefore it is suspected that the San Carlos olivine used here has some titanomagnetite impurities.

Both natural and synthetic olivines are known to include sub-micron iron-rich inclusions, such as magnetite (Belley et al., 2009). As such, their magnetic properties can be dominated by small amounts of such impurities, even when these impurities are too small to be seen with a visible microscope.

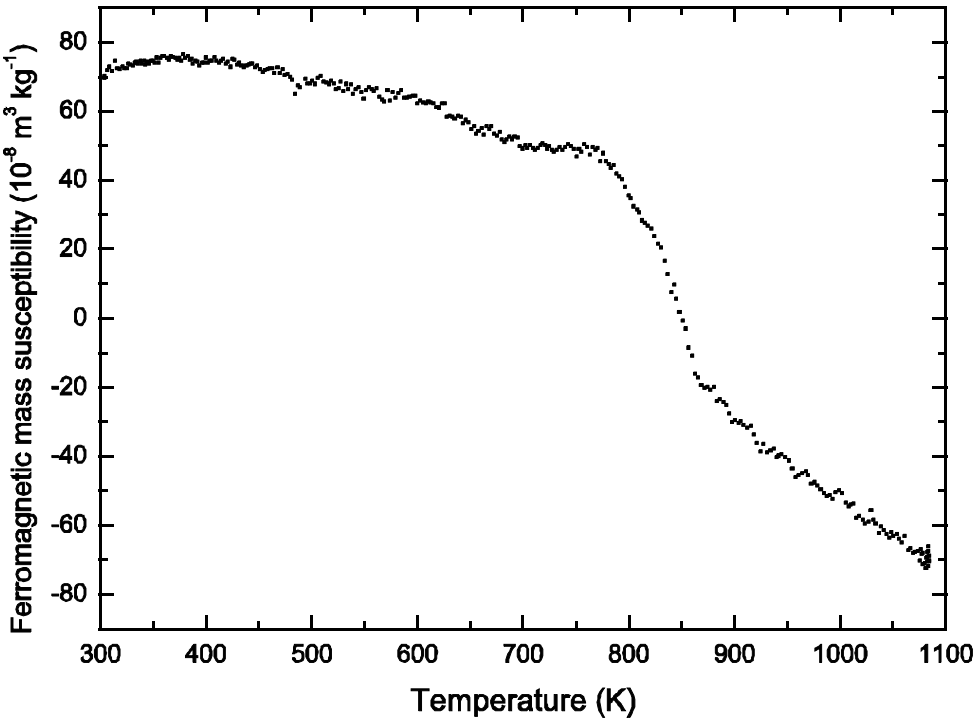

Figure 5. The ferromagnetic component of the magnetic susceptibility of San Carlos olivine during heating is plotted here. A pronounced drop in the susceptibility is seen in the region of 775 to 875 K.

In conclusion, TMA performed under the right conditions should enable the identification of all of the magnetic phases in a sample. However, for low levels of very fine grained metallic iron, it is difficult to prevent oxidation at high temperatures, which is what is believed happens here. It does not directly address the size distribution of the iron, although indications of magnetic blocking may be seen if SPM grains are present. In addition, although not attempted here, some attempts can be made to infer the size distribution from temperature dependant susceptibility, but prior assumptions are required about the form of the distribution function (Stephenson, 1971a, b).

6.3. Multi-frequency magnetic susceptibility

Ferromagnetic materials exhibit a complex magnetic behaviour dependent on grain size, for example internal subdivision into distinct magnetic domains in which magnetic dipoles are aligned. In large grains several such domains form in order to reduce magnetostatic energy, with neighbouring domains having opposing polarities, reducing the overall field. Such grains are known as multi-domain (MD). The smaller the grain, the fewer domains are evident until, at some point, the energy required to make a domain wall is greater than the saving in magnetostatic energy obtained by splitting a single domain into two. Below this critical size (which is a function of the grain shape and saturation magnetisation) the grains are all single domain (SD). It is these stable single domain grains that retain their magnetisation over geological timescales (see, for example, (Dunlop and Özdemir, 1997)).

Magnetised single domain grains exhibit a decay of remanent magnetisation over time, in an exponential process described by Equation 1, where J_{r0} is the initial remanent magnetisation, t is time and τ is the characteristic decay time, called the relaxation time.

$$J_r(t) = J_{r0} \exp\left(-\frac{t}{\tau}\right) \qquad \text{Equation 1}$$

The relaxation time (τ) is a measure of the time taken for a grain or domain to lose its acquired magnetisation after removal of the applied field. An expression for this parameter was derived by Néel (1949) and is shown in Equation 2, where v is the grain volume, h_c is the microscopic (theoretical) coercivity, j_s is the saturation magnetisation and kT is the thermal energy. The parameter f_0 is called the "frequency factor" and has a typical value of 10^9 s^{-1} (Nagata, 1961). In fact the expression in the exponential gives the ratio of the anisotropy energy to the thermal energy and can also be written as vK/kT where K is the anisotropy constant, and the microscopic coercivity is related to the saturation magnetisation and anisotropy constant by $h_c = 2K/j_s$. For magnetocrystalline anisotropy, $K = K_1/4$.

$$\tau = \frac{1}{f_0} \exp\left(\frac{v h_c j_s}{2kT}\right) = \frac{1}{f_0} \exp\left(\frac{Kv}{kT}\right) = \frac{1}{f_0} \exp\left(\frac{K_1 v}{4kT}\right) \qquad \text{Equation 2}$$

Single domain grains with very short relaxation times are known as superparamagnetic (SPM). From Equation 2 it can be seen that, for a given material, superparamagnetism occurs when either the grain is small enough or the temperature high enough. The definition of "short" is usually taken to mean the duration of a measurement, which varies according to the equipment used; 100 seconds for a typical laboratory experiment, 10^{-8} s for a Mössbauer measurement (the Larmor precession period for ^{57}Fe) or the oscillation period in an AC susceptibility measurement.

A superparamagnetic material will exhibit very strong magnetism and magnetic susceptibility in an applied field, but will lose this almost immediately when the field is removed. In this sense it behaves like a paramagnetic material, but with a much larger magnetic moment (hence the term superparamagnetism). Under the assumption that the grain is spherical (a fair approximation of metallic iron spherules in lunar soil, as seen from TEM measurements of grain rims (e.g. Pieters et al. (2000)) and taking the relaxation time to be 100 s, it is possible to calculate the grain diameter at which SD grains become SPM. Equation 2 is thus re-arranged for grain diameter, as in Equation 3.

In measurements of initial magnetic susceptibility using AC techniques, such as that employed by the Bartington instrument (described earlier), the measurement time can be taken as the reciprocal of the measurement frequency. Thus if a 1 kHz alternating field measurement is assumed, a time constant τ of order 10^{-3} s is found.

$$d = \left\{ \frac{12kT}{j_s h_c \pi} \ln\left(f_0 \tau\right) \right\}^{1/3} = \left\{ \frac{24kT}{K_1 \pi} \ln\left(f_0 \tau\right) \right\}^{1/3} \qquad \text{Equation 3}$$

For a spherical grain, as detected with ESR, magnetocrystalline coercivity is dominant (i.e. a perfectly spherical grain has no shape anisotropy), and a value of 4.8×10^4 J m^{-3} is typical for the first order cubic anisotropy constant and will be used here, although considerably higher values have been reported for iron nanoparticles (Lacroix et al., 2008). Substituting these values shows that the transition diameter between SPM and SD grains occurs at 20.3 nm. In other words, at a temperature of 300 K, grains smaller than this will be superparamagnetic, whilst those just slightly larger will be single domain ("magnetic blocking" is said to occur at 20.3 nm).

Changing the measurement frequency effectively shifts the grain size at which magnetic blocking occurs. For example, if the frequency is made 100 times larger, the transition size between SPM and SD particles will decrease to 19.0 nm for the example of iron at 300 K. This has the effect of making grains in the range 19.0 to 20.3 nm (previously SPM) now SD. The contribution of these grains to the total susceptibility is hence reduced and the measured susceptibility is less.

At the simplest level, room temperature measurements of magnetic susceptibility using an AC technique at two widely separated frequencies can detect the presence of superparamagnetic material. If a range of frequencies is available, magnetic granulometry can be performed. The Bartington MS2-B sensor is able to use two frequencies, 0.465 kHz and 4.65 kHz. This instrument was used to characterise the frequency response of the unaltered San Carlos olivine powder, in particular to look for signs of superparamagnetic magnetite or other ferromagnetic impurities. The results are presented in Table 3 and within experimental error, the susceptibilites at both high and low frequencies are identical, indicating that no significant superparamagnetic component is present. It has been demonstrated experimentally that a decrease in susceptibility of less than two percent per decade of frequency is measured if the material contains no SPM grains, a value in the range 10–14% is found for a sample containing virtually all SPM grains and a value in the middle has a mixture of SPM and coarser grains (Dearing, 1999).

	Initial susceptibility (10^{-8} m^3 kg^{-1})	
	Low frequency	High frequency
Unaltered	14.91 ± 0.12	14.86 ± 0.11
Irradiated	50.91 ± 0.24	48.70 ± 0.10

Table 3: Dual frequency magnetic susceptibility measurements of San Carlos olivine before and after irradiation. The irradiated material shows a decreased susceptibility at high frequencies, indicative of SPM material.

The same sample, measured again after irradiation, shows a greatly enhanced initial susceptibility and also pronounced frequency dependence, indicative of superparamagnetic material (Table 3). The measurement frequencies used by the Bartington instrument correspond to measurement times of 2.15 ms and 2.1 ms, giving blocking diameters of 20.7 nm and 19.5 nm for metallic iron. The decrease in susceptibility shows that there must be superparamagnetic grains present with sizes between these two limits. This compares well with the range of metallic iron grain sizes detectable by ESR spectroscopy (4 – 33 nm).

Despite being a useful technique for determining the presence of superparamagnetic material, multi-frequency measurements alone have a limited use for magnetic granulometry due to the weak dependence of the grain volume on τ in Equation 2. This is demonstrated in Figure 6 in which the SPM – SD transition diameter is plotted for a range of alternating field frequencies from 1 Hz to 1 GHz. Over this range the diameter only varies from 12.2 to 4.9 nm. Such measurements can be made in the laboratory, but as the frequency range is extended additional care has to be taken to consider the effects of sample conductivity. A considerable additional source of error is that the anisotropy constants and theoretical grain size boundaries for metallic iron and kamacite are not as well known as for, for example, magnetite, although recent theoretical studies have started to address this (Garrick-Bethell and Weiss, 2010).

In conclusion, multi-frequency measurements of AC magnetic susceptibility provide a rapid method of detecting the presence of SPM grains, but to make quantitative estimates of the sizes present, the magnetic carrier must first be identified. A considerably more useful technique would be to measure the frequency dependence of AC susceptibility at a range of temperatures, which not only expands the scope for magnetic granulometry by changing the blocking temperature, but enables identification of the magnetic phases by their Neél and Curie transitions. It has also been shown by Stephenson (1971a) that the frequency dependence of magnetic susceptibility can also be related to the grain size distribution, if some assumptions are made about the form of this distribution. Multi-frequency magnetic susceptibility measurements of *Apollo* 11 soils confirmed the distribution posited by other analyses. A more extensive characterisation of the weathered olivine samples over a range of frequencies would therefore be beneficial.

Finally, the measurements here detected the presence of a superparamagnetic component in the irradiated olivine samples that was not present in the starting material, but it cannot be uniquely attribute to metallic iron.

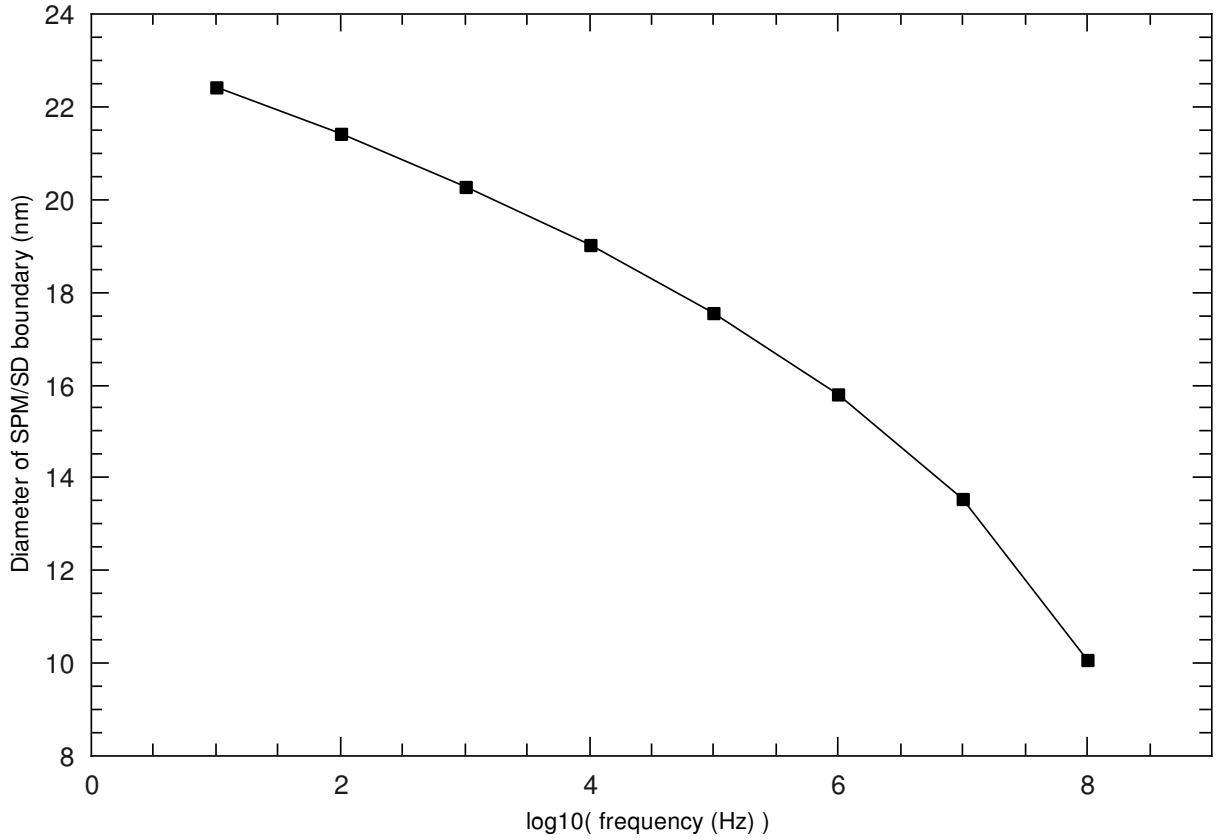

Figure 6. Plot of the grain size transition diameter between SPM and SD for metallic iron as a function of frequency at a temperature of 300 K.

6.4. Vibrating sample magnetometry

The measurement of initial magnetic susceptibility only accesses one portion of the hysteresis curve for a ferromagnetic material. Additional can be derived from investigating the entire hysteresis loop, i.e. by recording sample magnetism as a function of applied magnetic field. Figure 7 demonstrates a typical hysteresis loop, the degree of hysteresis exaggerated for clarity, and the parameters that can be derived from it.

An initially un-magnetised material plots at position 1 on the diagram. Small increases in applied field result in a reversible change and the gradient gives the initial susceptibility (χ_0), as measured by the Bartington instrument. The magnetisation increases with the field as shown until the saturation magnetisation (J_s) is reached at point 2. This occurs when all domains within a ferromagnetic material are aligned. For higher fields the $J(H)$ gradient is constant, representing the susceptibility of the paramagnetic component (χ_a).

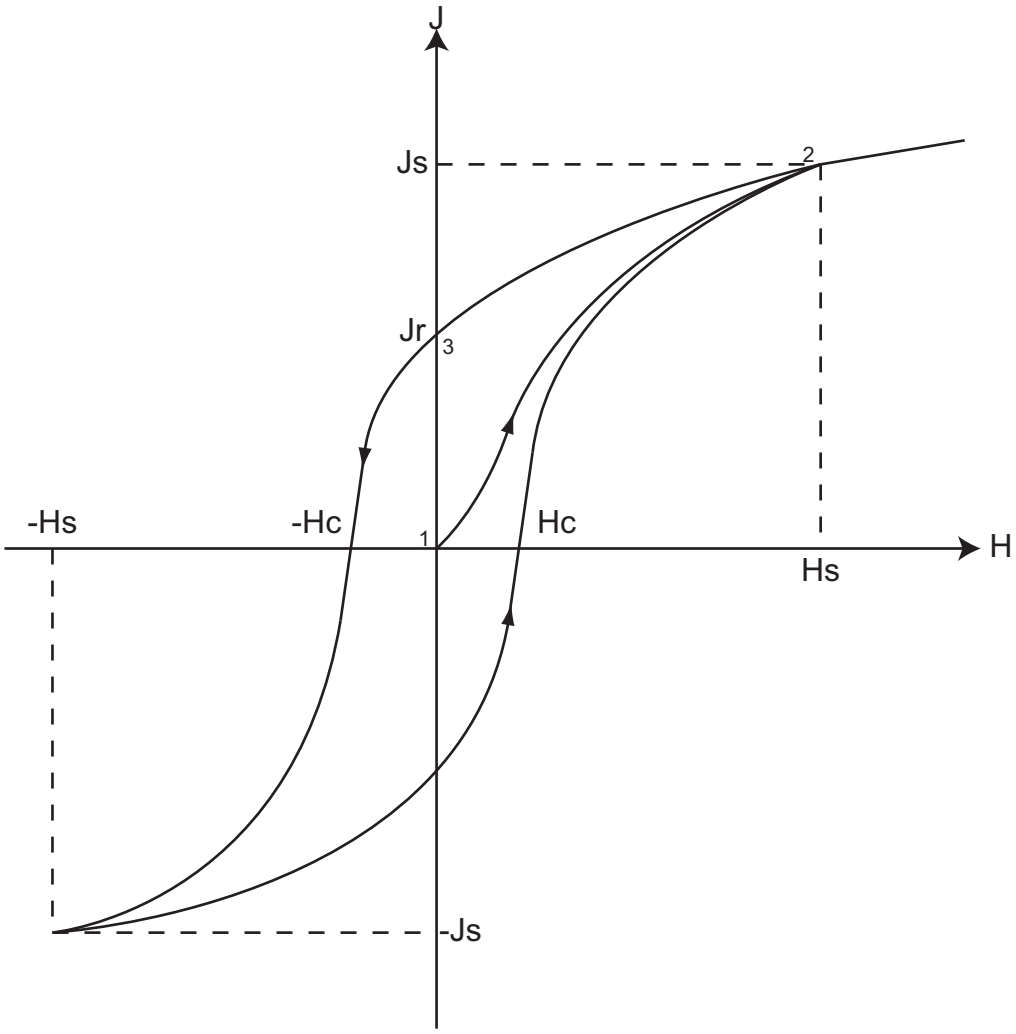

Figure 7. A schematic magnetic hysteresis curve showing the key derived parameters, including the saturation magnetisation (Js) and the coercive field (Hc).

If the magnetic field is now removed, a ferromagnetic material will still retain some remanent magnetisation (J_r), as at point 3. As the field is reversed, the magnetisation drops until it reaches zero. The field at which this occurs is called the coercive field (H_c) (also known as the coercivity or coercive force). If the field were removed at this point, some remanent magnetisation would still remain (although less than J_s since the sample would have been partially demagnetised). The reverse field that is that required to remove the saturation magnetisation completely is called the coercivity of remanence (H_r) and is always larger than the coercivity.

The shape of the curve in itself gives an excellent estimate of the dominant magnetic grain size of a sample. A broad hysteresis loop is indicative of a quantity of single domain grains, a sample with MD grains will have

a narrow loop and an ensemble of SPM particles should show no hysteresis. The similarity of MD and SPM loops at room temperature can be overcome by making additional low temperature measurements; grains which are superparamagnetic at room temperature become “blocked in” at lower temperature, and thus single domain.

The hysteresis parameters can be used to extract various useful properties, particularly if the ferromagnetic components have already been identified. The saturation magnetisation, for example, is proportional to the amount of magnetic material present. For lunar samples, Curie point measurements demonstrated that metallic iron and iron-nickel phases were the sole ferromagnetic components in both lunar rocks and soils (Fuller, 1998). Metallic iron has a saturation magnetisation of 218 $Am^2 kg^{-1}$ (Fuller, 1974) and thus the fraction of metallic iron in the lunar regolith can be calculated simply by dividing the measured saturation magnetisation by that of iron. Typical values of J_s for lunar fines are of order 1 $Am^2 kg^{-1}$, yielding a proportion of metallic iron of around half a percent by weight (Nagata et al., 1972) as discussed earlier.

The paramagnetic susceptibility of the sample is derived from the gradient of the hysteresis loop above the field required to saturate all ferromagnetic components. A value of 1 T is usually sufficient for most materials. For lunar rocks this measured paramagnetic component includes contributions from the Fe^{2+} in pure paramagnetic minerals, such as olivines and pyroxenes, and from antiferromagnetic minerals above their Néel temperature. An example of this is ilmenite ($FeTiO_3$), which has a Neél temperature of -210ºC; above this temperature ilmenite appears paramagnetic (Nagata et al., 1972). In lunar soils with significant amounts of SPM iron, it must be recalled that SPM materials appear paramagnetic and will also contribute to the high field susceptibility.

Magnetic hysteresis loops are most commonly measured on a vibrating sample magnetometer (VSM). This instrument is based principally on Faraday’s Law, in which an e.m.f. is induced in a measurement coil by a time-varying magnetic flux, produced by the movement of a magnetised sample. This measured signal is proportional to the magnetic moment of the sample. During this measurement an external magnetic field can be applied, usually by a powerful electromagnet designed to produce a very uniform field between its pole pieces. By combining these elements hysteresis loops can be recorded.

Measurements of this type were made using a Molspin VSM in the Centre for Environmental Magnetism and Paleomagnetism at Lancaster University. Samples of mass ~0.5 g of both unaltered and irradiated powder were weighed and wrapped in plastic film to prevent their movement during vibration and field application. Each was then tightly packed into a sample holder and loaded into the VSM.

If the unaltered San Carlos olivine were a pure sample, it should be paramagnetic at room temperature. Thus it should exhibit no hysteresis and plot as a straight line with a positive gradient. Hysteresis loop measurements are shown in Figure 8a for both the unaltered and irradiated samples. A field of 1 T was used. In both cases there is no clear hysteresis, and the unaltered sample is clearly dominated by paramagnetism; a straight line fit is possible with good confidence. There is thus no clear sign of a magnetic contaminant in these measurements.

The irradiated sample shows curvature at low fields, and a ferromagnetic component can potentially be extracted from this and analysed. Such analysis was performed using the HYSTEAR software (Von Dobeneck, 1996), which fits to the high field portion of the curve, extracting both the paramagnetic and ferromagnetic components, and finally derives the hysteresis parameters for the latter. A higher resolution curve was obtained of the irradiated sample with a maximum field of 300 mT. A fully modelled curve of the ferromagnetic component is shown in Figure 8b. Under the assumption that metallic iron is the source of this magnetic component, the saturation magnetisation of 10.3 Am^2/kg seen here can be used to calculate the amount of iron present as ~0.05 wt%. A Langevin fit can also be attempted to this presumed superparamagnetic component in order to find the mean magnetic grain size. This was attempted and a best fit achieved for a particle size of 1.3 nm, however the fit was poor at high field values; possibly more than one magnetic phase are contributing here, or the distribution of sizes is too broad to be fit with a single curve.

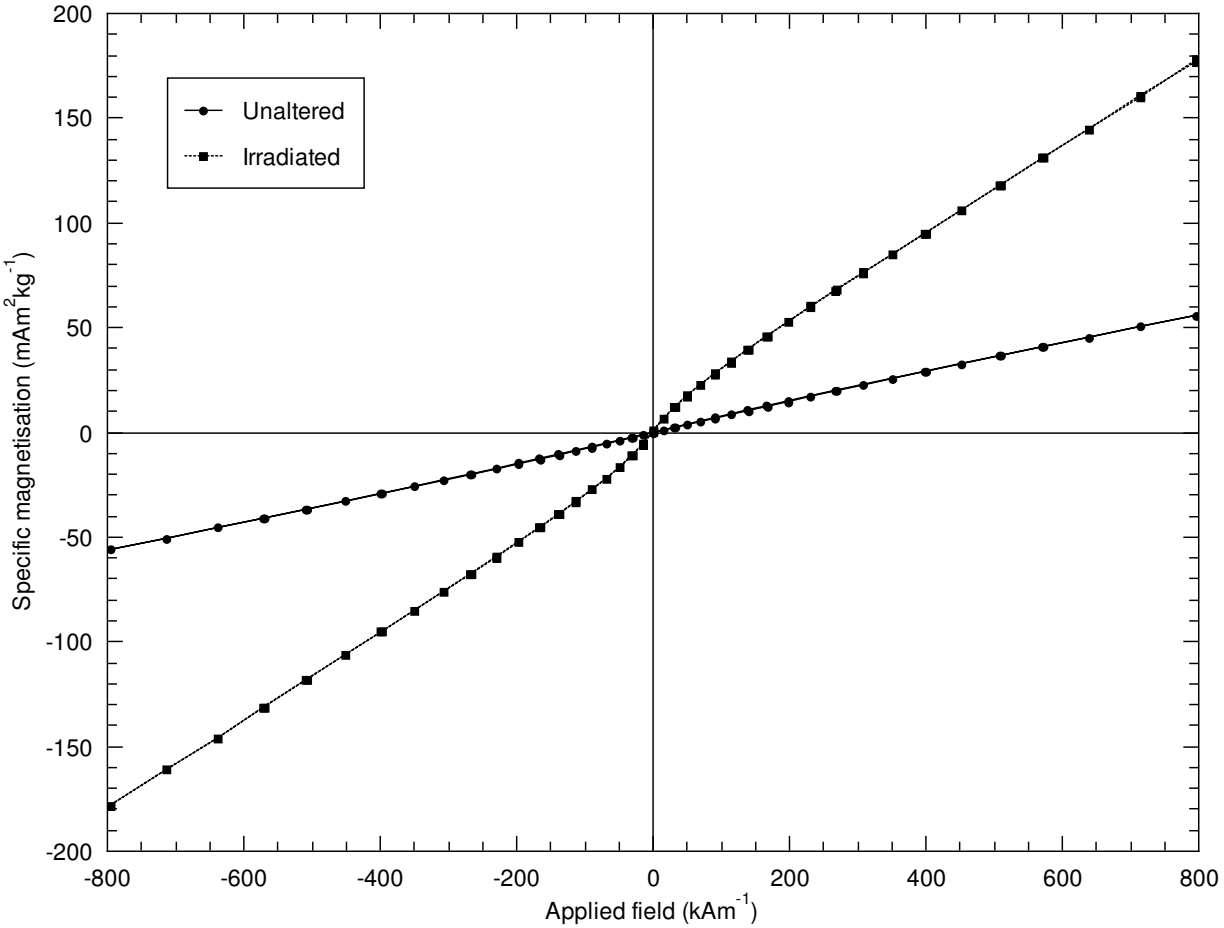

Figure 8a. Magnetic hysteresis curves for samples of unaltered and irradiated San Carlos olivine. The mass specific magnetisation is plotted against the applied field. The gradient of this curve at any point gives the mass specific magnetic susceptibility.

In conclusion, VSM measurements should be an excellent tool for determining the domain state of the magnetic component of a sample, once it has been identified. The similarity of SPM and MD hysteresis loops at room temperature can be overcome by making additional measurements at reduced temperature; if the curves are distinctly different, SPM material is present that appears as SD grains below their blocking temperature. In addition, the mean diameter of a collection of SPM grains can often be extracted by fitting a Langevin function where the grain volume is the only free parameter.

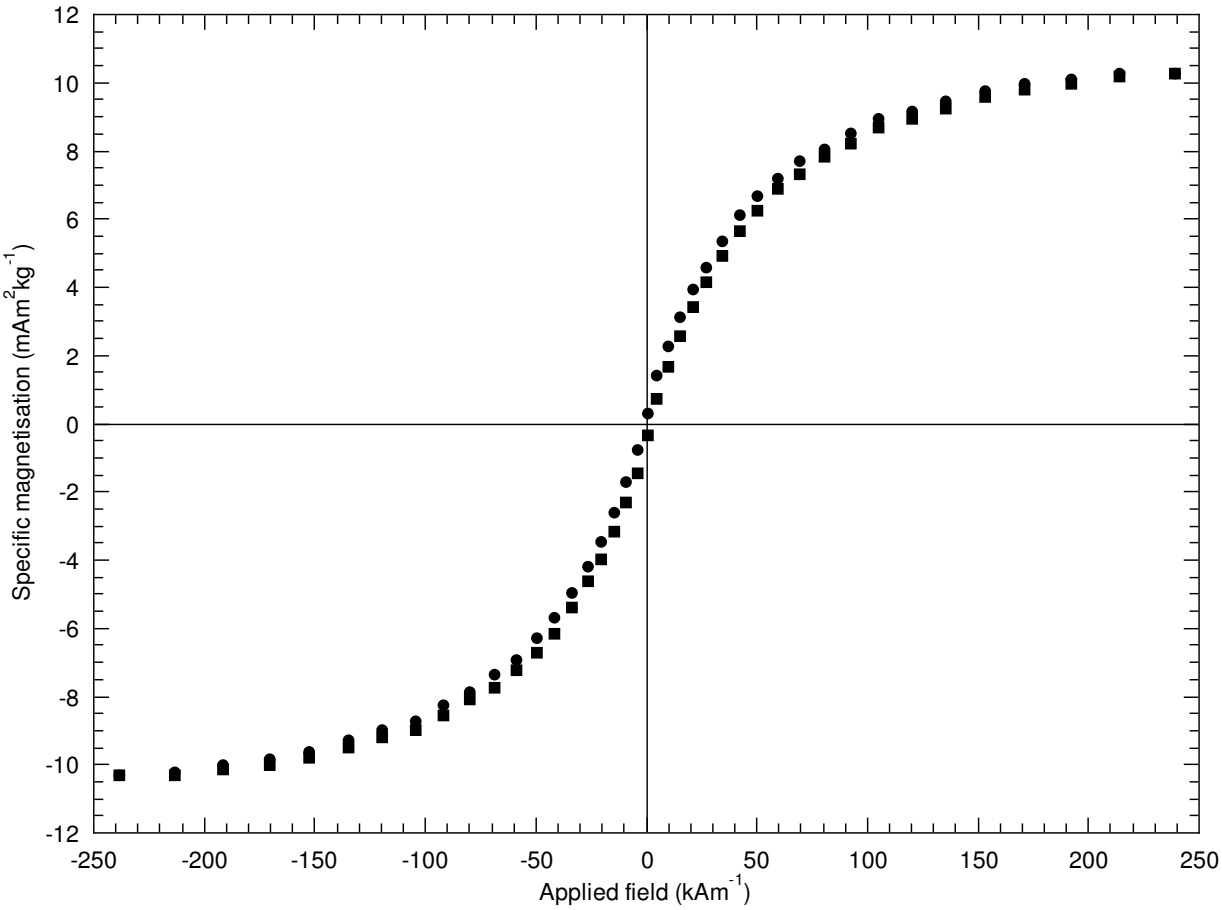

Figure 8b. A modelled hysteresis curve of the ferromagnetic component of the irradiated olivine sample. The different symbols represent the ascending and descending field directions.

The measurements here showed that the un-irradiated olivine samples exhibit almost pure paramagnetic behaviour. The irradiated sample has a weak ferromagnetic component which can be extracted and hysteresis parameters derived, although due to the previously detected presence of a magnetite-like phase it is possible that these parameters are not accurate.

6.5. Electron spin resonance

Although not a traditional rock magnetic technique *per se*, the next analysis discussed is ferromagnetic resonance (FMR). This has a particular heritage within the lunar soil community as one of the best maturity indices.

On analysis of the returned lunar samples, a variety of tracers were found in the soils that recorded their exposure to the surface environment (Langevin and Arnold, 1977). These included cosmic ray tracks, the metallic/ferrous iron ratio, magnetic susceptibility, the proportions of implanted solar wind noble gases and finally the ferromagnetic resonance signature, or I_s/FeO. The last of these was the most enduring since it has not been found to saturate with any lunar sample analysed to date.

Ferromagnetic resonance uses the same equipment as electron spin resonance (ESR), but applied to ferromagnetic materials. Paramagnetic and ferromagnetic materials, such as iron, have atoms with unpaired inner electrons. They therefore exhibit a net spin, angular momentum and magnetic moment. Under the application of an external magnetic field, these moments align themselves with the field, with spins either parallel or anti-parallel, and precess around it. The transition between these two states can be induced by application of electromagnetic radiation at the precession frequency, absorbing energy in doing so.

An absorption spectrum can be produced in this way. In practice, the microwave frequency is usually fixed and the magnitude of the external magnetic field varied to achieve resonance. An ESR spectrum is therefore a plot of the intensity received by a microwave detector as a function of the applied magnetic field. The intensity of a particular absorption feature believed due to metallic iron is measured (I_s) and normalise to the weight percentage of ferrous iron in the sample (FeO) to give the maturity index I_s/FeO. This last step is believed to be necessary because the amount of SMFe produced by space weathering must depend on the amount of source ferrous iron in the material. Thus some minerals are expected to weather more easily than others, and some, like quartz, not at all. A large number of lunar soils have been measured with this technique, and soils are classified into maturity grades according to their I_s/FeO. Typical values are less than 30 for immature soils, between 30 and 60 for sub-mature soils and up to 100 for mature soils (Morris, 1976).

Thus ferromagnetic materials can be identified and distinguished at a ppb level in bulk samples, with some constraints. At very small grain sizes, thermal disturbances overcome magnetic ordering and at large grain sizes, iron becomes multi-domain. FMR yields the amount of spherical metallic iron grains present within these limiting grain diameters, given as approximately 4 to 33 nm by Housley *et al.* (1976).

The olivine sample described previously was analysed in a Varian E109 ESR spectrometer, operating in the X-band at a frequency of 9 GHz with a 100 kHz field modulation. A few mg of the mineral powders were

loaded into a diamagnetic sample holder in each case. A mean field of 0.3 T was applied to compare bulk samples of olivine before and after irradiation. The derivative resonance spectrum produced (Figure 9) has a peak-to-peak line width (ΔH), of 65 nT and a *g*-factor of 2.10 ± 0.05, agreeing well with both lunar samples and previous weathering analogues (Morris 1978; Yamada et al. 1999). The *g*-factor is calculated from the relation $h\nu = g\mu_b B$, where v is the microwave frequency, μ_b is the Bohr magneton and B is the magnitude of the applied magnetic field. At the same (arbitrary) scale the unaltered sample is indistinguishable from the axis.

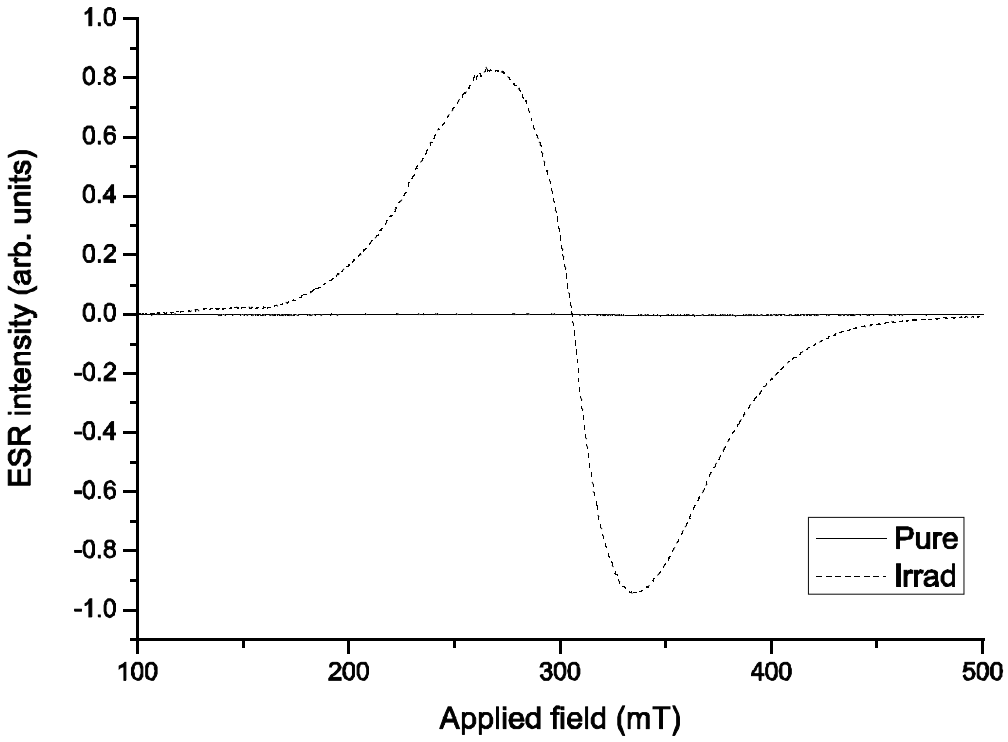

Figure 9. ESR spectrum of a San Carlos olivine sample before and after pulsed laser irradiation. The pure sample shows essentially no ESR signal at this scale, while the irradiated sample has a distinct resonance at a g-factor of 2.10 ± 0.05.

The laser irradiated olivine samples of Yamada et al. 1999) and Sasaki et al. 2002) have also been analysed by ESR spectroscopy (Kurahashi et al., 2002); (Sasaki et al., 2003) and showed similar results, with a g-factor of 2.10 ± 0.03 and a line-width of 70 mT. They also performed high resolution TEM and identified metallic iron in amorphous grain rims, to which they attributed the ESR signals.

Although not completely unambiguous, this gives a very good indication that spherical single domain metallic iron is being formed, some within the size range detectable via ESR (Morris, 1976). Having said that, the debate over the cause of the "characteristic resonance" in lunar fines was fierce during the early analyses of Apollo samples; both metallic iron and ferric oxides were considered as causes (Griscom, 1974). In any case, the product of irradiation here must be a single domain ferromagnetic carrier. This places some limits on the size of such particles. For a titanomagnetite, the limiting size of a single domain grain is between 80 nm and 200 nm (Dunlop and Özdemir, 1997), an order of magnitude larger than for metallic iron. One future method to distinguish between the magnetite-like and metallic iron sources for this signature would be to look at the temperature variation of the FMR signature between 10 and ~600 K (Griscom, 1980).

Assuming that metallic iron is present here, it would be useful to compare results of these experiments with the lunar maturity index I_s/FeO, where $I_s = (\Delta H)^2 A/m$, with ΔH and A being the peak-to-peak line-width and amplitude, respectively, and m the sample mass (Morris, 1977). However, since the amplitude is recorded in arbitrary units, cross-calibration of ESR spectrometers is required. It is hoped that a previously studied lunar regolith sample can be used to perform this calibration at a later date.

6.6. Summary of techniques

Table 4 collates the various magnetic methods used in this study, the parameters that can potentially be extracted from their use, and how they relate to the overall goal of measuring the quantity and size distribution of metallic iron in a given sample. In essence, the first task is to identify the magnetic component or components present in a sample. This can be done by measurements of the Curie point, however care must be taken to ensure that any fine-grained metallic iron present does not oxidise at high temperatures. A series of vibrating sample magnetometry runs at different temperatures should then be used to measure the amount of iron present (by its saturation magnetisation) and the dominant domain state (by the shape of the hysteresis curves and associated parameters). This places limits on the size distribution by comparison with the theoretically boundaries between SPM, SD and MD Fe^0 as a function of temperature. In addition, if SPM material is identified an average grain size can often be established by fitting a Langevin function to the data. Finally, a set of multi-frequency magnetic susceptibility measurements at a wide range of temperature can also help to plot the magnetic granulometry of a sample.

Technique	Parameters measured	Fe^0 size range	Unique detection of Fe^0?
Initial magnetic susceptibility	κ	Any (non specific)	No
Frequency dependant susceptibility	κ coefficient of frequency dependence (→ SPM present)	SPM/SD boundary, f(freq., T)	No
Vibrating sample magnetometry	$\kappa(B)$ j_s → wt% Fe^0	SPM, SD or MD. Can derive average size of SPM.	No
Thermomagnetic	Curie temperature → magnetic comopnent SPM size distribution	Any, can constrain SPM size via blocking temperature.	Yes
Electron spin resonance / FMR	g-factor → magnetic component Intensity → wt% Fe^0	all grains 4-33 nm	Possibly

Table 4. Summary of techniques

7. Conclusions and future work

In conclusion, an IR laser-ablation simulation facility was established to simulate space weathering on unconsolidated regolith simulants under a variety of temperature conditions. This facility was used to artificially weather samples of San Carlos olivine. As seen from previous experimental results, and the lunar regolith itself, changes result in the visible and near-infrared spectra, namely spectral darkening, reddening and reduced contrast.

The theoretical backgrounds of various magnetic techniques that can be used to describe the sub-microscopic iron content so critical for understanding space weathering were described, and these techniques applied to the weathering analogue. In order to further characterise the sub-microscopic iron content believed responsible for these optical changes, these magnetic analyses were performed. Although all techniques showed differences between the weathered and unweathered samples that could be attributed to SMFe, the quantity produced was insufficient for detailed analysis. In future experiments, repeated irradiation of the sample should be used to approach the lunar level of metallic iron (approximately 0.5 wt%).

In addition, a magnetic impurity was identified at low levels in the olivine sample, which made conclusive analysis of the magnetic measurements very difficult.

The experience gained from this work suggests a variety of improvements for similar experiments in the future:

1. Chips of olivine (or other starting mineral) should be measured with VSM initially to ensure that they have no magnetic impurities (i.e. that they plot as a straight paramagnetic line) before crushing. If the material is already in powdered form, magnetic separation could be used to remove high susceptibility grains.
2. Investigate the saturation effect with additional scans to further increase the proportion of sub-microscopic iron to lunar-like levels.
3. Attempt direct confirmation of the production of sub-microscopic iron, for example by measurement of the Curie point in a controlled H_2N_2 atmosphere. If more iron can successfully be produced by repeated irradiation, then sealing the sample under vacuum into a quartz holder might also suffice.
4. Detailed microscopic mineralogical analysis should be performed to describe in more detail the changes ascribed to the pulsed laser irradiation (e.g. melt versus vapour re-deposition).
5. It would also be interesting to perform acid-leaching experiments on the irradiated samples, to confirm the surface correlated nature of the changes in both optical and magnetic properties. This has been done for lunar samples (Hapke et al., 1970); if vapour deposition occurred in this weathering simulation, then removing the outer layer of material should also destroy the optical and magnetic signatures.
6. The ESR/FMR technique is very sensitive, however, since the amplitude is recorded in arbitrary units, cross-calibration of ESR spectrometers is required to compare with lunar I_s/FeO values. This could be achieved by measuring a lunar sample for which published results are available.
7. The frequency dependence of magnetic susceptibility could be further used to characterise the superparamagnetic component by extending the frequency range, and by measuring at a range of sample temperatures; reduced temperatures will allow magnetic ordering of material that is otherwise SPM at room temperature and above.

As a more philosophical point, in carrying out this work it became clear that there is a need for laboratories equipped to make these and the other measurements described in this paper. Such laboratories were prevalent in the post-*Apollo* era, but are not in common use (or existence!) today.

8. Acknowledgements

M.S. Bentley is grateful for PPARC (now STFC) for partially supporting this work, and wishes also to thank C.J. Harding for assistance with the ESR spectrometer, Carle Pieters and Takahiro Hiroi for producing reflectance spectra using the RELAB facility at Brown University and Dr V. Karloukovski for VSM measurements. RELAB is a multi-user facility supported by NASA grant NNG06GJ31G. The authors would also like to thank two anonymous reviewers for their extensive and insightful comments that greatly added to the quality of this manuscript.

References

Anselmi A., Scoon G.E., 2001. BepiColombo, ESA's Mercury Cornerstone mission. Planetary and Space Science 49 (14-15), 1409-1420.

Basu A., McKay D. S., Wentworth S. J.,2003. A Critical Examination of Relative Concentrations of Volume-correlated and Surface-correlated Submicron Globules of Pure Fe0 in Lunar Soils. Lunar and Planetary Science Conference 34, Abstract 1159.

Belley F., Ferré E. C., Martín-Hernández F., Jackson M. J., Dyar M. D., Catlos E. J., 2009. The magnetic properties of natural and synthetic $(Fe_x, Mg_{1-x})_2\ SiO_4$ olivines. Earth and Planetary Science Letters 284 (3-4), 516-526.

Bentley M. S., Ball A. J., Potter D. K., Wright I. P., Zarnecki J. C., 2009. In situ multi-frequency measurements of magnetic susceptibility as an indicator of planetary regolith maturity. Planetary and Space Science 57 (12), 1491-1499.

Blewett D.T., Robinson M.S., Denevi B.W., Gillis-Davis J.J., Head J.W., Solomon S.C., Holsclaw G.M., McClintock W.E., 2009. Multispectral images of Mercury from the first MESSENGER flyby: Analysis of global and regional color trends. Earth and Planetary Science Letters, 285 (3-4), 272-282.

Brunetto R., Romano F., Blanco A., Fonti S., Martino M., Orofino V., Verrienti C., 2006. Space weathering of silicates simulated by nanosecond pulse UV excimer laser. Icarus 180 (2), 546-554.

Carmichael, R., 1989. Handbook of Physical Properties of Rocks. CRC
Press Inc, Florida

Cintala M., 1992. Impact-Induced Thermal Effects in the Lunar and Mercurian Regoliths. Journal of Geophysical Research 97, 947-973.

Clark R., Roush T., 1984. Reflectance Spectroscopy: Quantitative Analysis Techniques for Remote Sensing

Applications. Journal of Geophysical Research 89 (B7), 6329-6340.

Cloutis E. A., Gaffey M. J.,1993. Lunar Regolith Analogues: Spectral Reflectance Properties of Compositional Variations. Icarus 102 (2), 203-224.

Dearing J., 1999. Environmental Magnetism: A Practical Guide. In: Walden, J., Oldfield, F., Smith, J.P. (Eds.), Environmental Magnetism: A Practical Guide. Quaternary Research Association, London.

Divine N., 1993. Five Populations of Interplanetary Meteoroids. Journal of Geophysical Research 98 (E9), 17,029-17,048.

Dunlop D. and Özdemir Ö., 1997. Rock Magnetism: Fundamentals and frontiers. Cambridge University Press, Cambridge.

Fuller M., 1974. Lunar Magnetism. Reviews of Geophysics and Space Physics 12 (1), 23-70.

Fuller M., 1998. Lunar magnetism - a retrospective view of the Apollo sample magnetic studies. Physics and Chemistry of The Earth 23 (7-8), 725-735.

Fuller M., Wu Y., Wasilewski P. J., 1975. The magnetic characteristics of returned lunar samples and their implications for regolith processes. Earth, Moon, and Planets 13 (1), 327-338.

Garrick-Bethell I., Weiss B.P., 2010. Kamacite blocking temperatures and applications to lunar magnetism. Earth and Planetary Science Letters 294, 1-7.

Greenwood N.N., Howe A.T., 1970. Mössbauer studies of Apollo 11 lunar samples. Geochimica et Cosmochimica Acta Supplement 1, 2163-2169.

Griscom D. L., 1974. Ferromagnetic resonance spectra of lunar fines: some implications of line shape analysis. Geochimica et Cosmochimica Acta 38 (10), 1509-1519.

Griscom D., 1980. Electron spin resonance in glasses. Journal of Non-Crystalline Solids 40 (1-3), 211-272.

Hapke B., 2001. Space weathering from Mercury to the asteroid belt. Journal of Geophysical Research 106 (E5), 10,039-10,074.

Hapke B.W., Cohen A.J., Cassidy W.A., Wells E.N., 1970. Solar radiation effects on the optical properties of Apollo 11 samples. Geochimica et Cosmochimica Acta Supplement 1, 2199.

Hill, D.C., 1990. The Micrometeoroid Impact Hazard in Space: Techniques for Damage Simulated by Pulsed Lasers and Environmental Monitoring. University of Kent, Unit for Space Sciences (PhD Thesis).

Hillier J. K., Sestak S., Green S., Postberg F., Srama R., Trieloff M., 2009. The production of platinum-coated silicate nanoparticle aggregates for use in hypervelocity impact experiments. Planetary and Space Science 57 (14-15), 2081-2086.

Hörz F., Cintala M. J., See T. H., Le L., 2005. Shock melting of ordinary chondrite powders and implications for asteroidal regoliths. Meteoritics and Planetary Science 40, 1329-1346.

Housley R.M., Cirlin E.H., Goldberg I.B., Crowe H.,1976. Ferromagnetic resonance studies of lunar core stratigraphy. In: Proceedings of the 7th Lunar Science Conference, 13-26.

Housley R.M., Grant R.W., Paton N.E., 1973. Origin and characteristics of excess Fe metal in lunar glass welded aggregates. In: Proceedings of the Fourth Lunar Science Conference, 2737-2749.

Hrouda F., 1994. A technique for the measurement of thermal changes of magnetic susceptibility of weakly magnetic rocks by the CS-2 apparatus and KLY-2 Kappabridge. Geophysical Journal International 118 (3), 604-612.

James C.L., Letsinger S.L., Basu A., Wentworth S.J., McKay D.S., 2003. Nanophase Iron Globules in Lunar Soil. Lunar and Planetary Science Conference 34, Abstract 1992.

Kadono T., Sugita S., Mitani N.K., Fuyuki M., Ohno S., Sekine Y., Matsui T., 2002. Vapor clouds generated by laser ablation and hypervelocity impact. Geophysical Research Letters 29 (20), 1979.

Keller L.P., Clemett S.J., 2001. Formation of Nanophase Iron in the Lunar Regolith. Lunar and Planetary Science Conference 32, Abstract 2097.

Keller L.P., Wentworth S.J., McKay D.S., Taylor L.A., Pieters C., Morris R.V., 2000. Space Weathering in the Fine Size Fractions of Lunar Soils: Mare/Highland Differences. Lunar and Planetary Science Conference 31, Abstract 1655.

Kissel J., Krueger F., 1987. Ion Formation by Impact of Fast Dust Particles and Comparison with Related Techniques. Applied Physics A 42, 69-85.

Kurahashi E., Yamanaka C., Nakamura K., and Sasaki S., 2002. Laboratory simulation of space weathering: ESR measurements of nanophase metallic iron in laser-irradiated materials. Earth Planets and Space 54 (12), e5-e8.

Lacroix L., Lachaize S., Falqui A., Blon T., Carrey J., Respaud M., Dumestre F., Amiens C., Margeat O., Chaudret B., Lecante P., Snoeck E, 2008. Ultrasmall iron nanoparticles: Effect of size reduction on anisotropy and magnetization. Journal of Applied Physics 103, 07D521-3.

Langevin Y., Arnold J., 1977. The Evolution of the Lunar Regolith. Annual Review of Earth and Planetary Sciences 5, 449-489.

Loeffler M.J., Dukes C.A., Baragiola R.A., 2009. Irradiation of olivine by 4 keV He^{+}: Simulation of space weathering by the solar wind. Journal of Geophysical Research 114, E03003.

Lucey P.G., Noble S.K., 2008. Experimental test of a radiative transfer model of the optical effects of space weathering. Icarus 197 (1), 348-353.

McDonnell J.A.M., Ashworth D.G., Flavill R.P., and Jennison R.C., 1972. Simulated microscale erosion on the lunar surface by hypervelocity impact, solar wind sputtering, and thermal cycling. In: Proceedings of the Third Lunar Science Conference 3, 2755-2765.

Melosh H., 1989. Impact Cratering: A Geologic Process. Oxford University Press.

Moroz L., Basilevsky A., Hiroi T., Rout S., Baither D., van der Bogert C., Yakovlev O., Fisenko A., Semjonova L., Rusakov V., Khramov D., Zinovieva N., Arnold G., Pieters C., 2009. Spectral properties of simulated impact glasses produced from martian soil analogue JSC Mars-1. Icarus 202 (1), 336-353.

Morris, R.V., 1976. Surface exposure indices of lunar soils - A comparative FMR study. In: Proceedings of the 7th Lunar Science Conference, 315-335.

Morris R.V., 1977. Origin and evolution of the grain-size dependence of the concentration of fine-grained metal in lunar soils - The maturation of lunar soils to a steady-state stage. In: Proceedings of the 8th Lunar Science Conference, 3, 3719-3747.

Morris R.V., 1978. The surface exposure (maturity) of lunar soils - Some concepts and I_s/FeO compilation. In: Proceedings of the 8th Lunar and Planetary Science Conference, 2, 2287-2297.

Müller M., Green S.F., McBride N., Koschny D., Zarnecki J.C., Bentley M.S. (2002) Estimation of the dust flux near Mercury. Planetary and Space Science 50 (10-11), 1101-1115.

Nagata T., 1961. Rock Magnetism. Maruzen Company Ltd., Tokyo.

Nagata T., Fisher R.M., Schwerer F.C., 1972. Lunar Rock Magnetism. Moon 4, 160-186

Néel L., 1949. Théorie du traînage magnétique des ferromagnétiques en grains fins avec application aux terres. Annales de Geophysique 5, 99-136.

Noble S.K., Pieters C.M., 2003. Space Weathering on Mercury: Implications for Remote Sensing. Solar System Research 37 (1), 31-35.

Noble S.K., Pieters C.M., Keller L.P., 2007. An experimental approach to understanding the optical effects of space weathering. Icarus 192 (2), 629-642.

Pieters C.M., Fischer E.M., Rode O., Basu A., 1993. Optical Effects of Space Weathering: The Role of the Finest Fraction. Journal of Geophysical Research 98 (E/11), 20,817-20,824.

Pieters C.M., Taylor L.A., Noble S.K., Keller L.P., Hapke B., Morris R.V., Allen C.C., McKay D.S., Wentworth S., 2000. Space weathering on airless bodies: Resolving a mystery with lunar samples. Meteoritics and Planetary Science 35 (5), 1101-1108.

Pieters C.M., Hiroi T., 2004. RELAB (Reflectance Experiment Laboratory): A NASA Multiuser Spectroscopy Facility. Lunar and Planetary Science Conference 35, Abstract 1720.

Pieters C.M., Klima R.L., Hiroi T., Dyar M.D., Lane M.D., Treiman A.H., Noble S.K., Sunshine J.M., Bishop J.L., 2008. Martian dunite NWA 2737: Integrated spectroscopic analyses of brown olivine. Journal of Geophysical Research 113, E06004.

Pirri A., 1977. Theory for laser simulation of hypervelocity impact. The Physics of Fluids 20 (2), 221-228.

Sasaki S., Hiroi T., Nakamura K., Hamabe Y., Kurahashi E., Yamada M., 2002. Simulation of space weathering by nanosecond pulse laser heating: dependence on mineral composition, weathering trend of asteroids and discovery of nanophase iron particles. Advances in Space Research 29 (5), 783-788.

Sasaki S., Kurahashi E., Yamanaka C., Nakamura K., 2003. Laboratory simulations of space weathering: changes of optical properties and TEM/ESR confirmation of nanophase metallic iron. Advances in Space Research 31 (12), 2537-2542.

Sasaki S., Nakamura K., Hamabe Y., Kurahashi E., and Hiroi T., 2001. Production of iron nanoparticles by laser irradiation in a simulation of lunar-like space weathering. Nature 410, 555-556.

Solomon S.C., McNutt Jr R.L., Gold R.E., Acuna M.H., Baker D.N., Boynton W.V., Chapman C.R., Cheng A.F., Gloeckler G., Head III J.W., 2001. The MESSENGER mission to Mercury: scientific objectives and implementation. Planetary and Space Science 49 (14-15), 1445-1465.

Sprague A., Emery J., Donaldson K., Russell R., Lynch D., Mazuk A., 2002. Mercury: Mid-infrared (3-13.5μm) observations show heterogeneous composition, presence of intermediate and basic soil types, and pyroxene. Meteoritics and Planetary Sciences 37, 1255-1268.

Stephenson A., 1971a. Single Domain Grain Distributions I. A Method for the Determination of Single Domain Grain Distributions. Physics of the Earth and Planetary Interiors 4, 353-360.

Stephenson A., 1971b. Single Domain Grain Distributions II. The Distribution of Single Domain Iron Grains in Apollo 11 Lunar Dust. Physics of the Earth and Planetary Interiors 4, 361-369.

Van de Moortèle B., Reynard B., Rochette P., Jackson M., Beck P., Gillet P., McMillan P., and McCammon C., 2007. Shock-induced metallic iron nanoparticles in olivine-rich Martian meteorites. Earth and Planetary Science Letters 262 (1-2), 37-49.

Von Dobeneck T., 1996. A systematic analysis of natural magnetic mineral assemblages based on modelling hysteresis loops with coercivity-related hyperbolic basis functions. Geophysical Journal International 124 (3), 675-694.

Wentworth S.J., Keller L.P., McKay D.S., and Morris R.V., 1999. Space weathering on the Moon: Patina on Apollo 17 samples 75075 and 76015. Meteoritics and Planetary Science 34 (4), 593-604.

Yamada M., Sasaki S., Nagahara H., Fujiwara A., Hasegawa S., Yano H., Hiroi T., Ohashi H., Otake H.,1999. Simulation of space weathering of planet-forming materials: Nanosecond pulse laser irradiation and proton implantation on olivine and pyroxene samples. Earth Planets and Space 51 (11), 1255-1265.